

Modelling the ocean site effect on seismic noise body waves

L Gualtieri, Éléonore Stutzmann, Véronique Farra, Yann Capdeville, M Schimmel, F Ardhuin, Andrea Morelli

▶ **To cite this version:**

L Gualtieri, Éléonore Stutzmann, Véronique Farra, Yann Capdeville, M Schimmel, et al.. Modelling the ocean site effect on seismic noise body waves. Geophysical Journal International, 2014, 197, pp.1096 - 1106. 10.1093/gji/ggu042 . insu-01396979

HAL Id: insu-01396979
https://insu.hal.science/insu-01396979

Submitted on 15 Nov 2016

HAL is a multi-disciplinary open access archive for the deposit and dissemination of scientific research documents, whether they are published or not. The documents may come from teaching and research institutions in France or abroad, or from public or private research centers.

L'archive ouverte pluridisciplinaire **HAL**, est destinée au dépôt et à la diffusion de documents scientifiques de niveau recherche, publiés ou non, émanant des établissements d'enseignement et de recherche français ou étrangers, des laboratoires publics ou privés.

Geophysical Journal International

Geophys. J. Int. (2014) **197,** 1096–1106
Advance Access publication 2014 March 7

doi: 10.1093/gji/ggu042

Modelling the ocean site effect on seismic noise body waves

L. Gualtieri,[1,2] E. Stutzmann,[1] V. Farra,[1] Y. Capdeville,[3] M. Schimmel,[4] F. Ardhuin[5] and A. Morelli[6]

[1] *Institut de Physique du Globe de Paris, Sorbonne Paris Cité, UMR* 7154 *CNRS, Paris, France. E-mail: gualtieri@ipgp.fr*
[2] *Dipartimento di Fisica e Astronomia, Settore di Geofisica, Università di Bologna, Bologna, Italy*
[3] *Laboratoire de Planétologie et Géodynamique de Nantes, CNRS, Université de Nantes, UMR-*6112*, France*
[4] *Institute of Earth Sciences Jaume Almera, CSIC, Lluis Sole i Sabaris s/n, E-*08028 *Barcelona, Spain*
[5] *Ifremer, Laboratoire d'Océanographie Spatiale, F-*29280 *Plouzané, France*
[6] *Istituto Nazionale di Geofisica e Vulcanologia, Bologna, Italy*

Accepted 2014 February 3. Received 2014 January 13; in original form 2013 July 15

SUMMARY

Secondary microseismic noise is generated by non-linear interactions between ocean waves at the ocean surface. We present here the theory for computing the site effect of the ocean layer upon body waves generated by noise sources distributed along the ocean surface. By defining the wavefield as the superposition of plane waves, we show that the ocean site effect can be described as the constructive interference of multiply reflected *P* waves in the ocean that are then converted to either *P* or *SV* waves at the ocean–crust interface. We observe that the site effect varies strongly with period and ocean depth, although in a different way for body waves than for Rayleigh waves. We also show that the ocean site effect is stronger for *P* waves than for *S* waves. We validate our computation by comparing the theoretical noise body wave sources with the sources inferred from beamforming analysis of the three seismogram components recorded by the Southern California Seismic Network. We use rotated traces for the beamforming analysis, and we show that we clearly detect *P* waves generated by ocean gravity wave interactions along the track of typhoon Ioke (2006 September). We do not detect the corresponding *SV* waves, and we demonstrate that this is because their amplitude is too weak.

Key words: Body waves; Site effects; Theoretical seismology.

GJI Seismology

1 INTRODUCTION

Microseisms are continuous oscillations of the ground with periods of between 3 and 20 s that can be detected worldwide (e.g. Gutenberg 1936; Webb 1998; Stutzmann *et al.* 2000; Berger 2004). They can be generated by the interactions among the atmosphere, the ocean and the solid Earth. Seismic noise spectra show two main peaks with periods of about 14 and 7 s, which are known as the primary and secondary microseisms, respectively.

The primary microseismic noise is the smaller amplitude hump that is generated by the interactions between the ocean gravity waves at a sloping seafloor, which occurs when the ocean waves reach shallow water. The corresponding seismic waves have the same period as the ocean gravity waves (Hasselmann 1963).

The secondary microseismic noise is the biggest peak in the noise spectra. Its generation is associated with the interactions between ocean gravity waves that have similar periods and are travelling in opposite directions. We can expect three possible sea-state configurations that result in secondary microseismic noise generation (Ardhuin *et al.* 2011). The first class occurs when a storm has a wide angular distribution, with ocean gravity waves coming from many different azimuths. This mechanism dominates at frequencies from 0.5 to 2 Hz, due to the wide angular distribution of the short waves generated by a constant and steady wind, and it can still be significant at lower frequencies. In this case, the interacting waves are within the storm. For the second class of sea-state configuration, ocean gravity waves arrive at the coast, where they are reflected and then meet up with incident ocean gravity waves. The interaction area is confined close to the coast. The third class of sea-state configurations relates to the interactions of ocean gravity waves coming from different storms. Ocean gravity waves from any given storm can travel long distances before meeting ocean gravity waves that are generated by another storm. This third class generates the strongest noise sources and these can occur anywhere in the ocean basin. Obrebski *et al.* (2012) showed an example of this third class of noise generation and located a source between Hawaii and California that was recorded by stations several thousands of kilometres away.

Secondary microseisms are mostly dominated by surface waves, and in particular by Rayleigh waves (Nishida *et al.* 2008). Theoretical studies of surface wave generation were developed by Miche (1944), Longuet-Higgins (1950) and Hasselmann (1963).

© The Authors 2014. Published by Oxford University Press on behalf of The Royal Astronomical Society.

Downloaded from http://gji.oxfordjournals.org/ at Biblio Planets on November 2, 2016

Recently, Gualtieri *et al.* (2013) demonstrated that the fundamental mode of Rayleigh waves is sufficient to explain the main features of the noise spectrum amplitude measured on the vertical component.

Over the past decades, many studies have focused on the location of surface wave sources. Rayleigh wave sources have been found in shallow water; that is, close to the coast (Bromirski & Duennebier 2002; Essen *et al.* 2003; Schulte-Pelkum *et al.* 2004; Gerstoft & Tanimoto 2007; Yang & Ritzwoller 2008), in deep water (Cessaro 1994; Stehly *et al.* 2006; Kedar *et al.* 2008; Obrebski *et al.* 2012) and in both cases (Haubrich & McCamy 1969; Friedrich *et al.* 1998; Chevrot *et al.* 2007). Stutzmann *et al.* (2012) modelled seismic noise surface waves in various environments and showed that the strongest noise sources are generated in deep water, whereas coastal reflection generates numerous smaller sources that contribute to the background noise level.

In this study, we deal with the noise body wave generation mechanisms in the band of the secondary microseismic period. The origin of noise body waves is still under debate. Sources of body waves have been found mostly by beamforming, which enables the determination of both the azimuth and the distance between a seismic network and a noise source. Probably, the first body wave source detection by beamforming appears to have been reported by Lacoss *et al.* (1969) and Haubrich & McCamy (1969). Several studies have demonstrated that a significant amount of *P*-wave microseismic energy is generated far from the coast in deep oceans (e.g. Gerstoft *et al.* 2008; Koper *et al.* 2009, 2010; Landès *et al.* 2010). Sources of body waves have also been associated with specific storms (e.g. Schulte-Pelkum *et al.* 2004; Gerstoft *et al.* 2006; Koper & de Foy 2008; Zhang *et al.* 2010a,b).

Specific phases have been detected by beamforming analysis. Zhang *et al.* (2009) and Koper *et al.* (2009, 2010) detected *P*-wave sources. Gerstoft *et al.* (2008) extracted *P*, *PP* and *PKP* sources. They compared the noise sources inferred by beamforming with ocean wave hindcast data, and they showed that these body wave microseisms are generated close to storms, where the ocean gravity waves are high. Koper & de Foy (2008) focused instead on body wave phases that have interacted with the Earth core: *PKP* and *PcP*.

A comparison between body wave sources in the primary and secondary microseismic frequency band was reported recently by Landès *et al.* (2010). They showed that sources of secondary and primary microseismic *P* waves do not coincide geographically, which indicates different generation mechanisms of these two microseismic peaks.

Hillers *et al.* (2012) compared body wave source locations inferred from beamforming and ocean wave model predictions, but they used the ocean site effect derived by Longuet-Higgins (1950) for Rayleigh waves. Differences in the spatial distribution of Rayleigh and body wave sources were observed by Obrebski *et al.* (2013) in the North Atlantic Ocean.

We use plane wave decomposition of the wavefield to study the body waves generated by the interactions between ocean gravity waves. Previous theoretical studies were developed by Vinnik (1973), who neglected the amplification effect of the water layer and Ardhuin & Herbers (2013), who included the water layer and used a local mode formalism. Here, we consider periods from 3 up to 10 s, and we demonstrate that the ocean site effect upon the wavefield is the result of constructive interference of multiply reflected *P* waves in the ocean, which are converted to either *P* waves or to *SV* waves at the seafloor. To compute the theoretical noise body wave sources, we consider the pressure field that acts at the ocean surface because of the gravity wave interaction, and we modulate this through the ocean site effect. These theoretical sources are compared with noise sources that are derived by beamforming analysis, for observed seismograms at the southern California seismic array. To identify the detected waves, we consider the three components and rotate them to analyse the beamforming along the *P*- and *SV*-components. In the Appendix, we show that the body wave site effect can also be obtained by using normal-mode theory. In the Appendix, we also show that the site effect acts differently on body wave and Rayleigh wave sources.

2 MODELLING OF THE OCEAN SITE EFFECT ON BODY WAVES

Seismic noise sources are due to non-linear interactions between ocean gravity waves and can be represented as a pressure field that acts on the ocean surface (Hasselmann 1963). To compute the seismic waves generated by this pressure field, it is possible to use the elastodynamic representation theorem (Aki & Richards 2002, chapter 2) written with the Green's function satisfying the free surface boundary conditions on the ocean surface. In our case, the sources are distributed along the ocean surface, so that only the surface integral term contributes to the expression of the representation theorem.

The Green's function can be decomposed as a sum of plane waves. For body waves in the far field, this sum can be approximated by using the stationary phase method; the corresponding expression is called the ray-theory Green's function, and this contains only the ray contributions. In this section, we use the plane wave decomposition of the Green's function, and compute the ocean site effect on one selected plane wave. As would be expected, only plane *P* waves are considered in the ocean layer.

We consider a 1-D model with an ocean layer and a homogeneous isotropic elastic crust below, which are in welded contact on a plane boundary (Fig. 1). We denote the velocity and density of the water layer with subscript 'w' and the velocity and density of the crust with subscript 'c'.

Let us consider a plane *P* wave that propagates inside the ocean layer from the top—which is the location of the microseismic source—to the bottom of the ocean. In the ocean layer, upgoing *P* waves are then generated by reflection at the seafloor and downgoing *P* waves by reflection at the free surface. At the seafloor, *P* and *S* waves are transmitted to the medium below. The angles θ_{P_w},

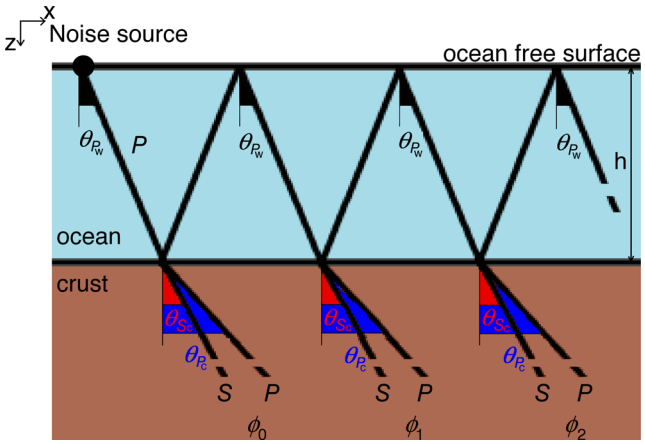


Figure 1. Cartoon illustrating the seismic rays that propagate from the source to the receiver. The reflection of *P* waves in the ocean layer and the transmission/conversion of *P* and *S* waves in the crust below are taken into account.

Downloaded from http://gji.oxfordjournals.org/ at Biblio Planets on November 2

θ_{P_c} and θ_{S_c} of the rays shown in Fig. 1 can be computed using Snell's law:

$$\frac{\sin\theta_{P_w}}{\alpha_w} = \frac{\sin\theta_{S_c}}{\beta_c} = \frac{\sin\theta_{P_c}}{\alpha_c} = p, \tag{1}$$

where p is the ray parameter.

Following Aki & Richards (2002), a plane P wave that propagates in a homogeneous layer (here the water layer) can be defined by its potential:

$$\phi_w(\mathbf{x}, t) = e^{[i(\mathbf{k}\cdot\mathbf{x}-\omega t)]} = e^{[i\omega(px+q_w z-t)]}, \tag{2}$$

where $\mathbf{k} = (k_x, k_z)$ is the wavenumber vector and $|\mathbf{k}| = |\omega/\alpha_w|$, where α_w is the compressional wave velocity in the ocean layer. We denote the spatial coordinates with $\mathbf{x} = (x, z)$ and time with t. Frequency and circular frequency are denoted as f and $\omega = 2\pi f$, respectively. The imaginary unit is denoted by 'i'. The horizontal and vertical slowness vector components are referred to as (p, q_w) and they are related to the propagation direction (defined by the angle θ_{P_w}) by the relation $(p, q_w) = (\frac{\sin\theta_{P_w}}{\alpha_w}, \frac{\cos\theta_{P_w}}{\alpha_w})$.

We consider first the case of the transmitted P waves. We denote with the index n the plane wave that is n times reflected from the free surface and n times reflected at the ocean bottom as a P wave before being transmitted from the seafloor in the medium below as a P wave. We call the reflection coefficient at the ocean bottom R and the P-wave transmission coefficient at the seafloor T_P. To compute the P-wave potential in the crust just under the ocean bottom, we can sum up the contributions of all of the P waves that are reflected in the water layer before being transmitted in the crust:

$$\begin{aligned}\phi_c(\mathbf{x}, t) &= \sum_{n=0}^{\infty} \phi_c^{[n]} = T_P(\theta_{P_w}) \sum_{n=0}^{\infty} \left[-R(\theta_{P_w})\, e^{i\Phi_w}\right]^n e^{i\omega(px+q_w h-t)} \\ &= C_p(\theta_{P_w}, h, \omega) e^{i\omega(px+q_w h-t)},\end{aligned} \tag{3}$$

where

$$C_P(\theta_{P_w}, h, \omega) = \frac{T_P(\theta_{P_w})}{1 + R(\theta_{P_w})\, e^{i\Phi_w(h,\omega,\theta_{P_w})}}. \tag{4}$$

The convergence of the series is guaranteed because $|R| < 1$. The minus sign before the coefficient R in the infinite sum is due to the reflection coefficient being (-1) on the free surface. We denote the phase shift due to the propagation within the water layer as Φ_w, which is defined as

$$\Phi_w(h, \omega, \theta_{P_w}) = 2\omega \frac{\cos\theta_{P_w}}{\alpha_w} h = 2\omega q_w h, \tag{5}$$

where h is the ocean depth (Fig. 1).

To obtain the reflection and transmission coefficients in terms of potentials for a solid/liquid interface, we impose that the normal displacement and the normal traction are continuous at the boundary between the ocean and the crust and that the tangential traction vanishes at the same discontinuity (e.g. Geldart & Sheriff 2004). The reflection coefficient R of the P wave at the liquid/solid interface is

$$R(\theta_{P_w}) = \frac{r_1 + r_2 - r_3}{r_1 + r_2 + r_3}, \tag{6}$$

in which

$$\begin{aligned} r_1 &= \rho_c \alpha_c (1 - 2p^2\beta_c^2)^2 \cos\theta_{P_w}, \\ r_2 &= 4\beta_c^3 p^2 \rho_c \sqrt{1 - p^2\alpha_c^2}\sqrt{1 - p^2\beta_c^2} \cos\theta_{P_w}, \\ r_3 &= \rho_w \alpha_w \sqrt{1 - p^2\alpha_c^2}. \end{aligned} \tag{7}$$

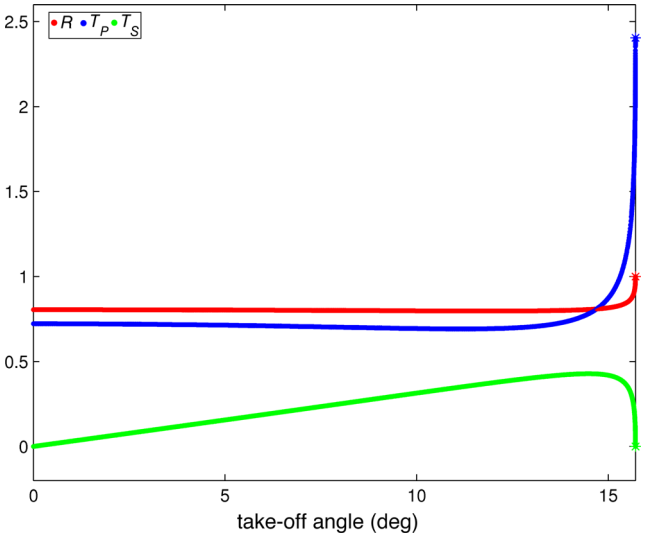


Figure 2. Plane wave reflection and transmission coefficients in terms of the potentials for the liquid–solid interface, with the incident wave being a P-wave propagating in the liquid. The P-to-P reflection and transmission coefficients are red and blue, respectively. The P-to-S transmission coefficient is green. The take-off angles are smaller than the P-wave critical angle $\theta^*_{P_w} \simeq 15.71^\circ$.

The P-to-P transmission coefficient T_P at the liquid/solid interface is

$$T_P(\theta_{P_w}) = \frac{2\rho_w \alpha_c \cos\theta_{P_w}(1 - 2p^2\beta_c^2)}{r_1 + r_2 + r_3}, \tag{8}$$

in which r_1, r_2 and r_3 are defined by eq. (7).

The same approach can be adopted for the P-to-S transmitted waves by setting in eq. (3) the P-to-S transmission coefficient T_S given by

$$T_S(\theta_{P_w}) = \frac{4\rho_w \beta_c^2 p \cos\theta_{P_w}\sqrt{1 - p^2\alpha_c^2}}{r_1 + r_2 + r_3}. \tag{9}$$

We note that in our simple 1-D model, the P-to-S transmitted waves at the ocean bottom will be SV waves.

In our computation, we use $\rho_w = 1.0\,\mathrm{g\,cm^{-3}}$ and $\alpha_w = 1.5\,\mathrm{km\,s^{-1}}$ for water density and P-wave velocity, respectively and $\rho_c = 2.5\,\mathrm{g\,cm^{-3}}$, $\alpha_c = 5.54\,\mathrm{km\,s^{-1}}$ and $\beta_c = \alpha_c/\sqrt{3} = 3.2\,\mathrm{km\,s^{-1}}$ for crust density and P- and S-wave velocities, respectively.

In Fig. 2, we show the coefficients R, T_P and T_S, which are given by eqs (6), (8) and (9). The results are shown for take-off angles smaller than the P-wave critical angle, as denoted by $\theta^*_{P_w} = \arcsin(\alpha_w/\alpha_c) \simeq 15.71^\circ$. For take-off angles larger than $\theta^*_{P_w}$, the reflection and transmission coefficients become complex. As we are not interested in evanescent waves, we consider only take-off angles smaller than $\theta^*_{P_w}$. Here, the coefficient T_S is always smaller than the coefficient T_P in the considered take-off angle range.

The coefficients R, T_P and T_S do not depend on ω for the water/rock discontinuity considered here. If a sediment layer is present between the water and the rock, frequency-dependent reflection and transmission coefficients can be introduced, which are obtained by following the approach of Červený (1989). This simple approach is valid if the thickness of the sediment layer is smaller than one half of the wavelength of the signal, which is the case under most of the oceans in the period range considered here.

We obtain the water-layer site effect upon P and S waves by summing up the site-effect coefficients for all the different take-off

Downloaded from http://gji.oxfordjournals.org/ at Biblio Planets on November 2, 2016

angles. Considering $C_P(\theta_{P_w}, h, \omega)$ given by eq. (4), for P waves we obtain

$$c_P(h,\omega) = \left(\int_0^{\theta^*_{P_w}} |C_P(\theta_{P_w}, h, \omega)|^2 \mathrm{d}\theta_{P_w} \right)^{1/2}, \quad (10)$$

and for S waves, we obtain

$$c_S(h,\omega) = \left(\int_0^{\theta^*_{P_w}} |C_S(\theta_{P_w}, h, \omega)|^2 \mathrm{d}\theta_{P_w} \right)^{1/2}, \quad (11)$$

where

$$C_S(\theta_{P_w}, h, \omega) = \frac{T_S(\theta_{P_w})}{1 + R(\theta_{P_w}) \mathrm{e}^{\mathrm{i}\Phi_w(h,\omega,\theta_{P_w})}}. \quad (12)$$

The coefficients in eqs (10) and (11) express the site effect due to the water layer upon the seismic wavefield generated by the noise sources. These coefficients are real numbers and vary with frequency and ocean depth; more precisely, they vary with the product fh. From results shown in Fig. 2, we can see that T_S is smaller than T_P in the whole take-off angle range, which means that c_S is always smaller than c_P.

3 QUANTITATIVE STUDY OF THE OCEAN SITE EFFECT UPON BODY WAVES

In this section, we investigate the ocean site effect upon body waves due to the combined effect of bathymetry h and frequency f. We consider the secondary microseismic period band; that is, periods from 3 to 10 s. We also vary the ocean depth from 1 to 10 km, to simulate the bathymetry.

In Fig. 3, we present the P- and S-wave coefficients as a function of the product fh/α_w, where f is the frequency, h is the ocean depth and α_w is the P-wave velocity in the ocean.

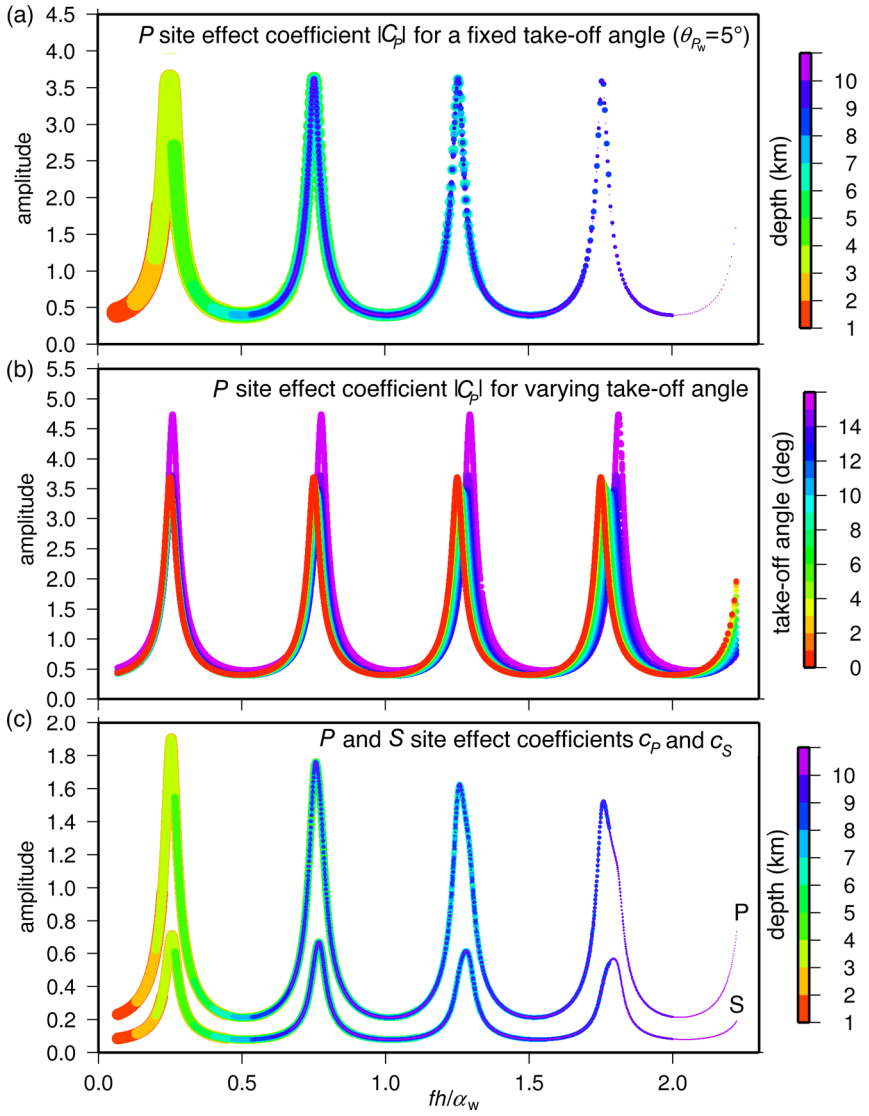


Figure 3. (a) Ocean site effect of P waves for a fixed take-off angle that corresponds to an epicentral distance of 60° for the direct P phase. The colour scale is related to bathymetry, showing that amplification occurs only at certain ocean depths. (b) P-wave site effect for take-off angles from 0° to 15° (colours). We observe that considering different ray parameters, we have small differences between the peak abscissas. (c) P- and S-wave site effects considering the integration over all of the take-off angles (ocean depth in colour). We observe peaks at close abscissas, meaning that they are related to similar combinations of depth and frequency.

Downloaded from http://gji.oxfordjournals.org/ at Biblio Planets on November 2

Table 1. Take-off angle θ_{P_w} (fourth column) computed for each seismic phase (first column) in a given range of epicentral distance (second column). In the third column, we show the corresponding ray parameters. All of these take-off angles are included in our computation of the ocean site-effect coefficients c_P and c_S.

Seismic wave	Epicentral distance Δ (deg)	Ray parameter p (s km^{-1})	Take-off angle θ_{P_w} (deg)
P	30°–95°	0.041–0.080	3.524–6.85
PP	60°–180°	0.042–0.080	3.59–6.86
PKP	143°–175°	0.030–0.040	2.54–3.44
PcP	0°–70°	0.0009–0.038	0.074–3.27
S	30°–95°	0.080–0.141	6.72–12.22
SS	60°–190°	0.083–0.141	7.14–12.22
SKS	110°–144°	0.019–0.037	1.62–3.20
ScS	0°–70°	0.002–0.071	0.14–6.11

Fig. 3(a) shows the *P*-wave coefficient $|C_P|$ for the take-off angle $\theta_{P_w} = 5^\circ$, which corresponds to the epicentral distance of about 60° for the direct *P* phase. The ocean depth is marked with different colours. It can be seen that only some combinations of frequency and ocean depth give strong amplification $|C_P|$. Considering that the average worldwide ocean depth is around 4 km, we are mostly interested in the first two peaks.

In Fig. 3(b), we show the *P*-wave coefficient $|C_P|$ for take-off angles between 0° and 15° (in colours), with 1° steps. We observe that the abscissas of the first two resonant peaks are relatively similar for the different take-off angles. Prominent differences occur for the last two peaks, which correspond to relatively unusual ocean depths (i.e. greater than 6 km in depth). Different seismic phases are related to different take-off angles. In Table 1, we show the take-off angles θ_{P_w} (fourth column) for different seismic phases (first column) in a given range of epicentral distances (second column). We observe that all of the seismic phases are related to take-off angles smaller than $\theta^*_{P_w}$. A specific phase can therefore be extracted by considering the appropriate ray parameter range.

Fig. 3(c) shows the site-effect coefficients c_P and c_S, given by eqs (10) and (11), respectively. Ardhuin & Herbers (2013) obtained a similar result by using local modes in a flat medium. Here, by decomposing the wavefield into a sum of plane *P* waves, we show that the ocean site effect is the result of the constructive interferences of *P*-wave multiples reflected in the ocean.

In the Appendix, we show that the same result can be obtained by using normal modes and selecting them in relation to the seismic phase. The computation of the site effect for Rayleigh waves was reported by Gualtieri *et al.* (2013, their fig. 2). In Fig. A1, we compare the site effect for Rayleigh waves (A1b) and body waves (A1a) by plotting their amplitude as a function of fh/α_w. We observe a strong difference in shape between body wave and Rayleigh wave site effects, which means that their most amplified sources are potentially located in different geographical regions.

To determine the oceanic regions that produce the strongest site effect on body waves, we show maps of the site-effect coefficients c_P and c_S, given by eqs (10) and (11), at different periods. In Fig. 4, we show maps for *P* waves (left-hand column) and *S* waves (right-hand column) for three fixed periods: 4, 5 and 6 s. We use different colour scales for the *P* and *S* waves, because the coefficient for *P* waves is larger than that for *S* waves. We observe strong site-effect variability with period. At 4 s, the maximum site effect occurs for depths of 1.5 and 4.5 km, which correspond to the maxima of the first two peaks in Fig. 3(c). Depths around 4.5 km correspond to wide areas of the ocean basins (Fig. 4). For a period of 5 s, the maxima of the first two peaks (Fig. 3c) correspond to depths of 1.9 and 5.7 km. The area of strong site effects are different from those observed at period of 4 s, with much stronger amplification in northwest Atlantic Ocean close to Canada and in the Pacific Ocean close to Japan (Fig. 4). Finally, for a period of 6 s, the maximum site effect corresponds to depths of 2.3 and 6.8 km (Fig. 3c). Bathymetry of 6.8 km is rare in the ocean and therefore mostly ridges and coastal areas amplify the noise source (Fig. 4). For that period, only the first peak of Fig. 3(c) is important. The existence of two peaks of high amplification explains the strong variability of the ocean site effect with period.

4 NOISE BODY WAVE SOURCES

We compute the theoretical noise body wave sources by considering the pressure field $P(f)$ due to the interaction of the ocean gravity waves and by taking into account the site effect computed in Section 2. The modulus of the pressure field is given by

$$|P(f)| = A\sqrt{F_p(\mathbf{K} \simeq 0, f)}, \tag{13}$$

where $F_p(\mathbf{K} \simeq 0, f)$ is the spectral density of the pressure field at the ocean surface due to the ocean wave–wave interaction (Hasselmann 1963; Ardhuin *et al.* 2011), and A is a normalization constant that depends on the sampling parameters used in the ocean wave model. The spectral density $F_p(\mathbf{K} \simeq 0, f)$ is given by

$$F_p(\mathbf{K} \simeq 0, f) = \rho_w^2 g^2 f E^2(f/2) \int_0^\pi M(f/2, \theta) M(f/2, \theta + \pi) \mathrm{d}\theta, \tag{14}$$

where ρ_w is the water density, g is the gravity acceleration, $f/2$ is the ocean wave frequency, $\mathbf{K}$ is the sum of the wave numbers of the two opposite ocean gravity waves, $E(f)$ is the sea surface elevation variance and $M(f, \theta)$ is the non-dimensional ocean gravity–wave energy distribution as a function of the ocean gravity–wave frequency f and the azimuth θ. To compute the spectral density $F_p(\mathbf{K} \simeq 0, f)$, we use the ocean wave model that was developed by Ardhuin *et al.* (2011). This is a global scale model with a constant resolution of 0.5° in both latitude and longitude. One key point of this model is that it is the only model to date that takes into account the coastal reflection of ocean gravity waves. In our computation, we consider 5 per cent coastal reflection.

We then compute the *P*- and *S*-wave noise sources as products of the modulus of the pressure field $|P(f)|$ (eq. 13) and the mean site-effect coefficients $\bar{C}_P = c_P/\theta^*_{P_w}$ and $\bar{C}_S = c_S/\theta^*_{P_w}$ for the *P* and *S* waves, respectively. The unit of noise body wave sources is then Pa · s.

Downloaded from http://gji.oxfordjournals.org/ at Biblio Planets on November 2, 2016

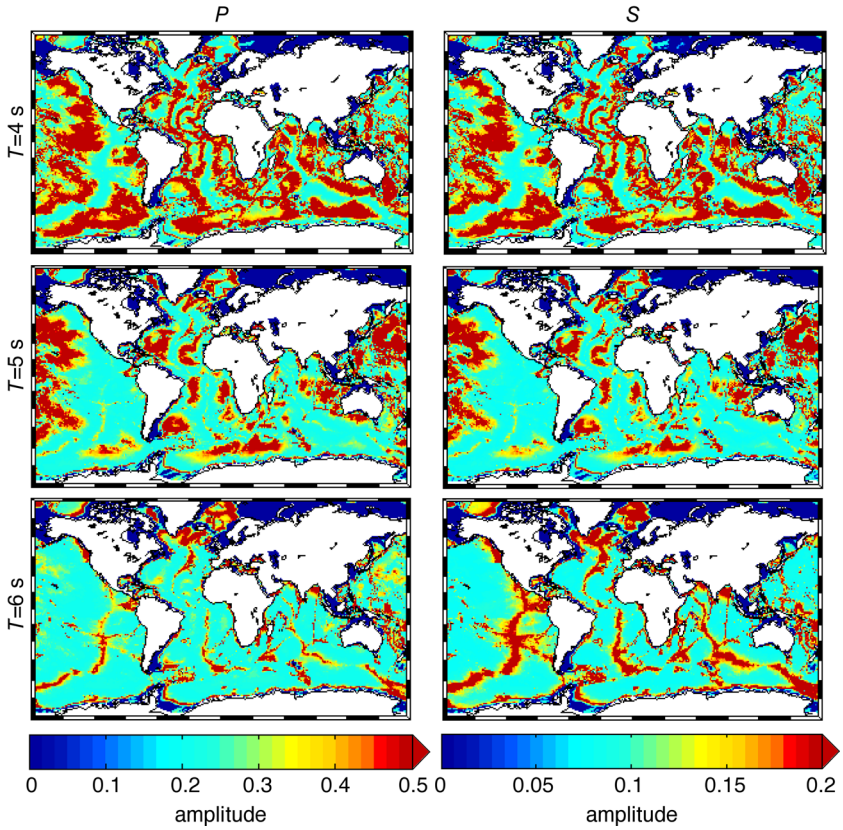


Figure 4. Maps of the ocean site-effect coefficients c_P (left-hand column) and c_S (right-hand column) as a function of the period: 4 s (first row), 5 s (second row) and 6 s (third row). The same colour scale is used for the same wave type.

In Fig. 5, we present the example of the Typhoon Ioke in the western Pacific. Figs 5(a) and (b) show the significant wave height and the bathymetry (from Amante & Eakins 2009). Figs 5(c) and (d) show the modelled wave interaction for a period of 5 s, averaged over 2 hr on the day of 2006 September 4 (Julian day 247) and the *P*-wave ocean site-effect coefficient c_P as computed by eq. (10). Figs 5(e) and (f) show the corresponding *P*- and *S*-wave theoretical sources. For a typhoon, the noise sources are class I; that is, generated by the interactions of the ocean waves associated with the typhoon. Therefore, the strongest wave interactions are in the vicinity of the largest significant wave height. The significant wave height maximum corresponds to the typhoon location, and its successive positions define the typhoon track. The comparison of Figs 5(a) and (c) shows that the largest wave interactions occur along the typhoon track and behind the typhoon. The largest wave interactions are in the typhoon tail, and the distance between the locations of the significant wave height maximum and wave interaction maximum varies with the displacement velocity of the typhoon. Zhang *et al.* (2010b) used a beamforming approach on the southern California network data to follow this typhoon track over several days. They computed the beam power from the vertical component seismograms, and they backprojected the beam maximum slowness, under the assumption that the corresponding wave is a *P* wave. They showed good agreement between the typhoon track and the backprojected source location.

In Fig. 5(b), we show that the bathymetry does not change significantly along the typhoon track. Because of that, at a fixed period of $T = 5$ s, the ocean site effect c_P does not vary strongly along the typhoon track too (Fig. 5d). From Fig. 4, we also observe that the amplification due to the ocean site effect is strong only at the period of $T = 5$ s along the typhoon track.

To validate our modelling, we analyse the Typhoon Ioke data recorded by the Southern California Seismic Network (network code CI), and we consider the three-component seismograms. We compute the beamforming power spectrum for an angular frequency ω as follows:

$$BF(\omega, \mathbf{s}) = |\sum_{i=1}^{N_s} S_i(\omega) e^{-i\omega \mathbf{s}\cdot(\mathbf{x}_i - \mathbf{x_c})}|^2, \quad (15)$$

where N_s is the number of stations, $S_i(\omega)$ is the seismogram spectrum that is recorded at station i, $\mathbf{s}$ is the slowness vector towards the source, $\mathbf{x}_i$ is the position vector of station i and $\mathbf{x_c}$ is the position vector of the network centre. In Fig. 6(a), we show the beam power spectrum computed from the vertical seismograms over the same 2-hr time window as in Fig. 5. We observe a maximum for the slowness modulus of 0.053 s km^{-1} and the azimuth of 290.8°.

To determine which wave type corresponds to the detected slowness, we rotate the vertical, north and east components into the so-called *P, SV* and transverse components. The radial (*R*) and transverse (*T*) components are the horizontal components towards the source and perpendicular, respectively. For each slowness vector, $\mathbf{s}$, we first rotate the north and east components towards the radial and transverse components (Fig. 6b). We then rotate the vertical and radial components towards the *P* and *SV*-components (Fig. 6c). The angle of rotation is the *P*-wave theoretical angle of incidence i, which is computed for each slowness $s = ||\mathbf{s}||$ using $s = \sin i/\alpha$, where α is the *P*-wave velocity at the receivers. We take $\alpha = 5$ km s^{-1}.

Downloaded from http://gji.oxfordjournals.org/ at Biblio Planets on November 2

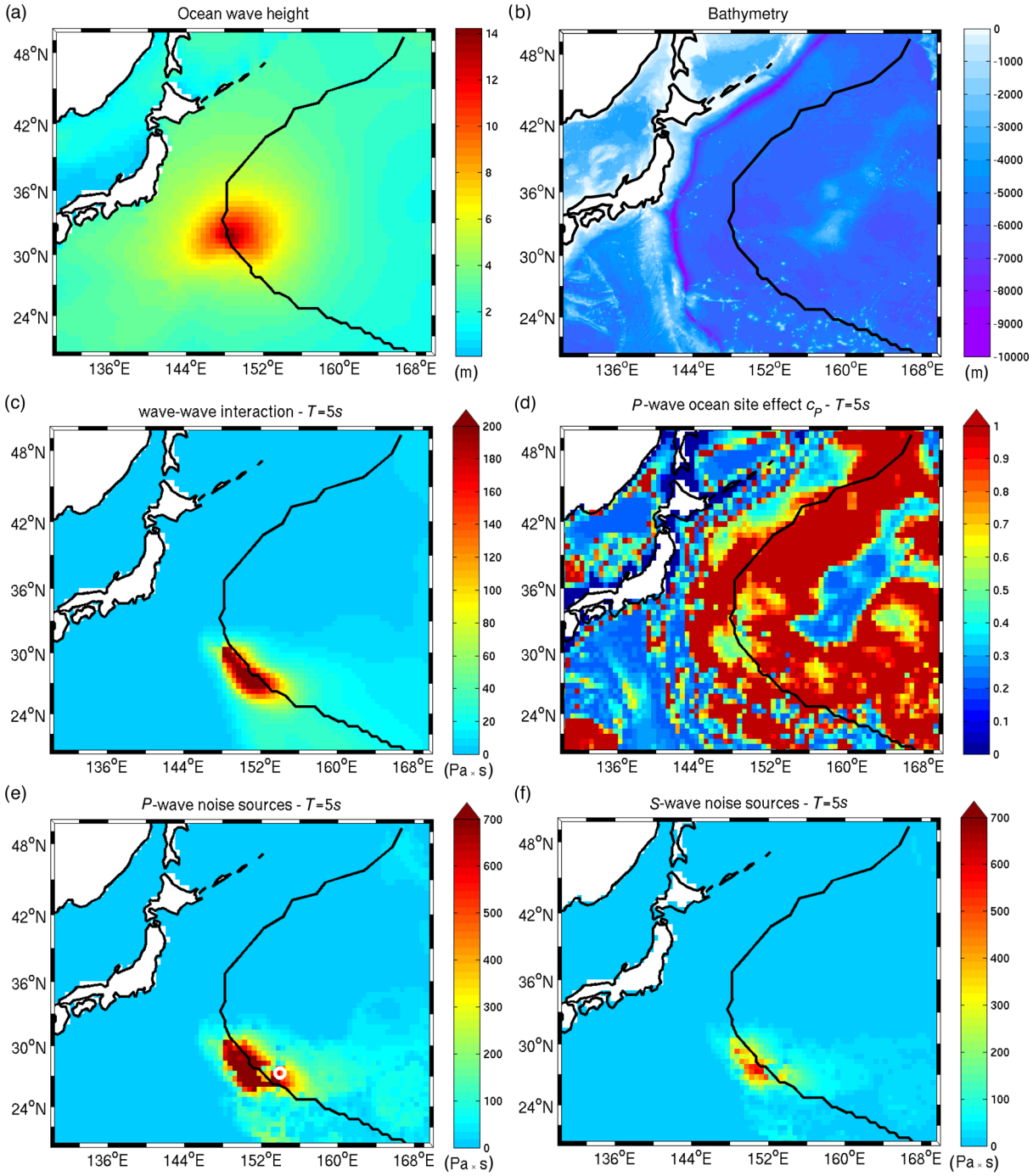


Figure 5. Typhoon Ioke on 2006 September 4, 12:00–14:00. The typhoon track is plotted with the black line. (a) Significant wave height. (b) Bathymetry (from Amante & Eakins 2009). (c) Modulus of the pressure field spectrum $|P(f)|$ due to the interaction of the ocean gravity waves. (d) *P*-wave ocean site effect c_P. (e) Theoretical noise sources for the *P* waves. The white circle shows the location of the *P*-wave source detected by beamforming analysis. (f) Theoretical noise sources for the *SV* waves. Figs (c), (d), (e) and (f) are computed at a period of 5 s.

Incoming *P* waves are mostly polarized along the *P*-component, and incoming *SV* waves are mostly polarized along the *SV*-component. For each slowness, we compute the beamforming power spectrum (BF) of the *P*, *SV* and *T* components using eq. (15). In Figs 6(d) and (e), we show the *P*-component and *SV*-component BF. For the *P*-component, we observed a BF maximum at the slowness 0.0529 s km^{-1} and azimuth of 292.2°, which are very close to those values obtained from the vertical component BF. The maximum amplitude is 0.9 relative to the vertical component BF maximum. We find the *P*-wave source location by backprojecting the slowness and azimuth, and we obtain the source coordinates (27.33°N, 153.96°E). We observe good agreement with the *P*-wave source derived from the wave model (Fig. 5e). On the *SV*-component BF (Fig. 6e), we observe an extremum at the same slowness and azimuth as on the *P* and vertical component BFs. Its amplitude is 0.23 relative to the vertical component BF maximum, which is much weaker than the

Downloaded from http://gji.oxfordjournals.org/ at Biblio Planets on November 2, 2016

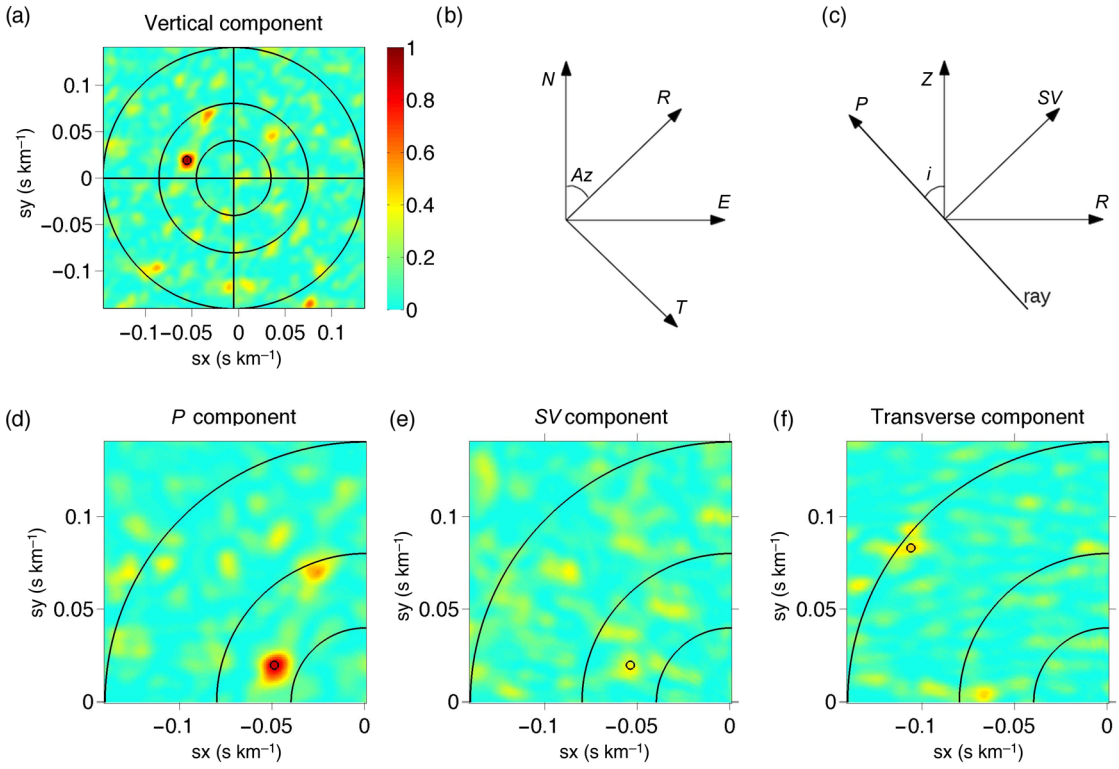


Figure 6. (a) Beamforming power spectrum of the vertical component seismograms. The colour scale is normalized to the vertical component maximum. (b), (c) Cartoon of the coordinates. The *Z*-axis is vertical and the *R*-axis is horizontal towards the network-source azimuth. The *P* and *SV*-axes are in the vertical plane defined by *Z* and *R*. The *P*-axis is towards the theoretical direction of the incident *P* wave, and the *SV*-axis is perpendicular to *P*. The *P*-component (d), *SV*-component (e) and *T*-component (f) beamforming power spectra. The small black circles indicate the beam maximum. The large black circles and circle arcs correspond to slownesses of 0.04, 0.08 and 0.14 s km^{-1}. For a distance range of 30° to 90°, the *P*-wave slowness is between 0.04 and 0.08 s km^{-1}, and the *S*-wave slowness is between 0.08 and 0.14 s km^{-1}.

amplitude detected on the *P*-component BF. We interpret this signal as the result of the *P*-to-*SV* conversions under the receivers. From theory, we would also expect to observe an *SV* wave generated at the same source location as the *P* wave. This would correspond to a beam maximum at the slowness of 0.1 s km^{-1} along the azimuth of 292°, but it is not observed on the *SV*-component BF (Fig. 6e). The relative amplitude of the *S* wave with respect to the *P* wave is given by

$$A_{S/P} = \frac{\exp(-\pi t_s^*/T)}{\exp(-\pi t_p^*/T)} \frac{\sqrt{J_p}}{\sqrt{J_s}} \left(\frac{C_S}{C_P} \frac{\alpha_c}{\beta_c} \right), \tag{16}$$

where subscripts *S* and *P* are for the *S* and *P* waves, respectively, *T* is the period, t^* characterizes the seismic attenuation along the path, $\sqrt{J}$ is the geometrical spreading, *C* is the ocean site effect computed with eqs (4) and (12) and α_c and β_c are the *P*- and *S*-wave velocities in the crust, respectively. The ratio α_c/β_c converts the relative ocean site effect C_S/C_P from potential to displacement. The relative geometrical spreading effect is about 1. For the period of 5 s, the relative ocean site effect is $C_S/C_P = 0.33$ and the relative seismic attenuation effect along the path is 0.17; we obtain $A_{S/P} \simeq 0.1$. We estimate the *SV*-component BF relative noise level at 0.15. Therefore, it is impossible to detect the generated *SV*-wave signal of relative BF amplitude $0.1^2 = 0.01$ because it is too far below the noise level. Finally, we checked that we do not observe any *SH*-wave on the transverse component BF at the theoretical slowness of 0.1 s km^{-1} and the azimuth of 292.2° (Fig. 6f).

5 CONCLUSION

In this study, we used the plane wave superposition of the wavefield to compute the site effect of the ocean layer upon seismic noise body waves. We considered only seismic waves in the secondary microseismic period band. We demonstrate that the ocean site effect can be modelled by considering the constructive interferences of multiply reflected *P* waves in the ocean, which are converted into *P* and *SV* waves at the liquid–solid seafloor interface. We show in the Appendix that the noise body wave site effect can also be retrieved using normal modes.

We computed both the *P*- and *S*-wave ocean site effects and we observe that they have the same dependence with respect to frequency and bathymetry. Fixing the period, we show site-effect maps where the amplification patterns are relatively similar for both *P* and *S* waves. However, in terms of amplitude, these maps show a stronger site effect for the *P* waves than for the *S* waves. We also observe important variations with frequency of the site-effect maps for the same seismic phase. The Rayleigh wave site effect was recently computed by Gualtieri *et al.* (2013) using normal modes. Comparing Rayleigh wave and body wave site effects (see the Appendix), we observe that the local bathymetry produces a different effect on these.

We validate our modelling by computing noise theoretical sources as the product of the pressure field induced by the interaction of ocean gravity waves and the site-effect coefficient. We compare our results with the beamforming analysis results for Typhoon Ioke (2006 September) that was recorded by the Southern California Seismic Network. To identify which waves correspond to the BF

Downloaded from http://gji.oxfordjournals.org/ at Biblio Planets on November 2

detected signals, we rotated the traces to compute the *P*, *SV* and transverse component BF. We obtain a good match between the theoretical and observed noise source detected on the vertical and *P*-component beamforming power spectra, which confirms that it is a *P* wave. For the same slowness and azimuth, we also detect a signal on the *SV*-component BF. We interpret this as the result of the *P*-to-*S* conversions in the crust under the seismic array. On the *SV*-component BF, we do not detect any signal at the *S*-wave slowness corresponding to the same source. We demonstrate that the amplitude of the generated *SV* wave is too small to be detected on the *SV*-component BF.

The computation of the noise body wave site effect can be used to investigate the body wave source locations in detail, and to compare body wave and Rayleigh wave noise sources. This can also be used to investigate the energy levels of noise body waves in the secondary microseismic period band. Moreover, the introduction of a sedimentary layer between the ocean and the crust might affect the body wave source amplification, especially close to the coast, and its study should be the subject of future studies.

ACKNOWLEDGEMENTS

We acknowledge the support of the QUEST Initial Training Network funded within the EU Marie Curie Programme. MS acknowledges financial support through the projects Rifsis (CGL 2009-09727) and Topolberia (CSD2006-00041). Most of the figures were prepared using Generic Mapping Tools (GMT; Wessel & Smith 1995). We thank the two anonymous reviewers for their detailed comments that helped us to improve our manuscript. This is IPGP contribution number 3498.

REFERENCES

Aki, K. & Richards, P.G., 2002. *Quantitative Seismology,* 2nd edn, University Science Books.

Amante, C. & Eakins, B.W., 2009. *ETOPO1 1 Arc-Minute Global Relief Model: procedures, data sources and analysis, NOAA Technical Memorandum NESDIS NGDC-24,* 1–19.

Ardhuin, F. & Herbers, T.H.C., 2013. Noise generation in the solid Earth, oceans and atmosphere, from nonlinear interacting surface gravity waves in finite depth, *J. Fluid Mech.,* **716,** 316–348.

Ardhuin, F., Stutzmann, E., Schimmel, M. & Mangeney, A., 2011. Ocean wave sources of seismic noise, *J. geophys. Res.,* **116**(C9), C09004, doi:10.1029/2011JC006952.

Berger, J., 2004. Ambient Earth noise: a survey of the global seismographic network, *J. geophys. Res.,* **109**(B11), B11307, doi:10.1029/2004JB003408.

Bromirski, P.D. & Duennebier, F.K., 2002. The near-coastal microseism spectrum: spatial and temporal wave climate relationships, *J. geophys. Res.,* **107**(B8), 2166–2185.

Červený, V, 1989. Synthetic body wave seismograms for laterally varying media containing thin transition layers, *Geophys. J. R. astr. Soc.,* **99**(2), 331–349.

Cessaro, R.K., 1994. Sources of primary and secondary microseisms, *Bull. seism. Soc. Am.,* **84**(1), 142–148.

Chevrot, S., Sylvander, M., Benahmed, S., Ponsolles, C., Lefèvre, J.M. & Paradis, D., 2007. Correction to 'Source locations of secondary microseisms in western Europe: evidence for both coastal and pelagic sources", *J. geophys. Res.,* **112**(B12), B12398, doi:10.1029/2007JB005481.

Dziewonski, A.M. & Anderson, D.L., 1981. Preliminary reference Earth model, *Phys. Earth planet. Inter.,* **25**(4), 297–356.

Essen, H.-H., Krüger, F., Dahm, T. & Grevemeyer, I., 2003. On the generation of secondary microseisms observed in northern and central Europe, *J. geophys. Res.,* **108**(B10), doi:10.1029/2002JB002338.

Friedrich, A., Krüger, F. & Klinge, K., 1998. Ocean-generated microseismic noise located with the Gräfenberg array, *J. Seismol.,* **2**(1), 47–64.

Geldart, L.P. & Sheriff, R.E., 2004. *Problems in Exploration Seismology and Their Solutions,* Society Of Exploration Geophysicists.

Gerstoft, P. & Tanimoto, T., 2007. A year of microseisms in southern California, *Geophys. Res. Lett.,* **34**(20), L20304, doi:10.1029/2007GL031091.

Gerstoft, P., Fehler, M.C. & Sabra, K.G., 2006. When Katrina hit California, *Geophys. Res. Lett.,* **33**(17), L17308, doi:10.1029/2006GL027270.

Gerstoft, P., Shearer, P.M., Harmon, N. & Zhang, J., 2008. Global P, PP, and PKP wave microseisms observed from distant storms, *Geophys. Res. Lett.,* **35**(23), L23306, doi:10.1029/2008GL036111.

Gualtieri, L., Stutzmann, E., Capdeville, Y., Ardhuin, F., Schimmel, M., Mangeney, A & Morelli, A., 2013. Modelling secondary microseismic noise by normal mode summation, *Geophys. J. Int.,* **193**(3), 1732–1745.

Gutenberg, B., 1936. On microseisms, *Bull. seism. Soc. Am.,* **26**(2), 111–117.

Hasselmann, K., 1963. A statistical analysis of the generation of microseisms, *Rev. Geophys.,* **1**(2), 177–210.

Haubrich, R.A. & McCamy, K., 1969. Microseisms: coastal and pelagic sources, *Rev. Geophys.,* **7**(3), 539–571.

Hillers, G., Graham, N., Campillo, M., Kedar, S., Landes, M. & Shapiro, N., 2012. Global oceanic microseism sources as seen by seismic arrays and predicted by wave action models, *Geochem. Geophys. Geosyst.,* **13**(1), doi:10.1029/2011GC003875.

Kedar, S., Longuet-Higgins, M., Webb, F., Graham, N., Clayton, R. & Jones, C., 2008. The origin of deep ocean microseisms in the North Atlantic Ocean, *Proc. R. Soc. A,* **464**(2091), 777–793.

Koper, K.D. & de Foy, B., 2008. Seasonal anisotropy in short-period seismic noise recorded in South Asia, *Bull. seism. Soc. Am.,* **98**(6), 3033–3045.

Koper, K.D., de Foy, B. & Benz, H., 2009. Composition and variation of noise recorded at the Yellowknife Seismic Array, 1991–2007, *J. geophys. Res.,* **114**(B10), B10310, doi:10.1029/2009JB006307.

Koper, K.D., Seats, K. & Benz, H., 2010. On the composition of Earth's short-period seismic noise field, *Bull. seism. Soc. Am.,* **100**(2), 606–617.

Lacoss, R.T., Kelly, E.J. & Toksöz, M.N., 1969. Estimation of seismic noise structure using arrays, *Geophysics,* **34**(1), 21–38.

Landès, M., Hubans, F., Shapiro, N.M., Paul, A. & Campillo, M., 2010. Origin of deep ocean microseisms by using teleseismic body waves, *J. geophys. Res.,* **115**(B5), B05302, doi:10.1029/2009JB006918.

Longuet-Higgins, M.S., 1950. A theory of the origin of microseisms, *Phil. Trans. R. Soc. Lond., A,* **243**(857), 1–35.

Miche, A., 1944. Mouvements ondulatoires de la mer en profondeur croissante ou décroissante. Première partie. Mouvements ondulatoires périodiques et cylindriques en profondeur constante, *Ann. Ponts Chaussées,* **114,** 42–78.

Nishida, K., Kawakatsu, H., Fukao, Y. & Obara, K., 2008. Background Love and Rayleigh waves simultaneously generated at the Pacific Ocean floors, *Geophys. Res. Lett.,* **35**(16), L16307, doi:10.1029/2008GL034753.

Obrebski, M., Ardhuin, F., Stutzmann, E. & Schimmel, M., 2013. Detection of microseismic compressional (P) body waves aided by numerical modeling of oceanic noise sources, *J. geophys. Res.,* **118**(8), 4312–4324.

Obrebski, M.J., Ardhuin, F., Stutzmann, E. & Schimmel, M., 2012. How moderate sea states can generate loud seismic noise in the deep ocean, *Geophys. Res. Lett.,* **39**(11), L11601, doi:10.1029/2012GL051896.

Schulte-Pelkum, V., Earle, P.S. & Vernon, F.L., 2004. Strong directivity of ocean-generated seismic noise, *Geochem. Geophys. Geosyst.,* **5**(3), doi:10.1029/2003GC000520.

Stehly, L., Campillo, M. & Shapiro, N.M., 2006. A study of the seismic noise from its long-range correlation properties, *J. geophys. Res.,* **111**(B10), B10306, doi:10.1029/2005JB004237.

Stutzmann, E., Roult, G. & Astiz, L., 2000. GEOSCOPE station noise levels, *Bull. seism. Soc. Am.,* **90**(3), 690–701.

Stutzmann, E., Ardhuin, F., Schimmel, M., Mangeney, A. & Patau, G., 2012. Modelling long-term seismic noise in various environments, *Geophys. J. Int.,* **191**(2), 707–722.

Vinnik, L.P., 1973. Sources of microseismic P waves, *Pure appl. Geophys.,* **103**(1), 282–289.

Webb, S.C., 1998. Broadband seismology and noise under the ocean, *Rev. Geophys.,* **36**(1), 105–142.

Downloaded from http://gji.oxfordjournals.org/ at Biblio Planets on November 2, 2016

Wessel, P. & Smith, W.H.F., 1995. New version of the Generic Mapping Tools released, EOS, Trans. Am. geophys. Un., **76**(33), 329.
Yang, Y. & Ritzwoller, M.H., 2008. Characteristics of ambient seismic noise as a source for surface wave tomography, *Geochem. Geophys. Geosyst.,* **9**(2), doi:10.1029/2007GC001814.
Zhang, J., Gerstoft, P. & Shearer, P.M., 2009. High-frequency P-wave seismic noise driven by ocean winds, *Geophys. Res. Lett.,* **36**(9), L09302, doi:10.1029/2009GL037761.
Zhang, J., Gerstoft, P. & Bromirski, P.D., 2010a. Pelagic and coastal sources of P-wave microseisms: generation under tropical cyclones, *Geophys. Res. Lett.,* **37**(15), L15301, doi:10.1029/2010GL044288.
Zhang, J., Gerstoft, P. & Shearer, P.M., 2010b. Resolving P-wave travel-time anomalies using seismic array observations of oceanic storms, *Earth planet. Sci. Lett.,* **292**(3–4), 419–427.
Zhao, L. & Dahlen, A., 1995. Asymptotic normal modes of the Earth—II. Eigenfunctions, *Geophys. J. Int.,* **121,** 1–42.
Zhao, L & Dahlen, F.A., 2007. Asymptotic eigenfrequencies of the Earth's normal modes, *Geophys. J. R. astr. Soc.,* **115**(3), 729–758.

APPENDIX: NOISE BODY WAVE SITE EFFECT USING NORMAL MODES

We develop here a method for retrieving the noise body wave site effect using normal modes, and we compare the result with the site effect computed using plane wave superposition.

Considering noise sources as vertical point forces at the top of the ocean, Gualtieri *et al.* (2013) provided the expression of the site-effect coefficients using normal-mode theory:

$$c_n = \frac{{}_n\mathrm{U}_l(\mathbf{r_r})\,{}_n\mathrm{U}_l(\mathbf{r_s})}{{}_n\omega_l}, \tag{A1}$$

where ${}_n\omega_l$ is the angular frequency, and ${}_n\mathrm{U}_l$ is the radial eigenfunction for a mode described by quantum numbers (n, l). The receiver and source positions are denoted by $\mathbf{r_r}$ and $\mathbf{r_s}$, respectively.

Body waves are generated by the constructive interaction of high-order overtones. To identify the normal modes that provide a contribution to the generation of a specific seismic phase, we use the ray parameter. In a spherically symmetric earth model, the ray parameter is defined as $p = r\sin i(r)/v(r)$, where $v(r)$ is the seismic velocity field computed at distance r from the centre of the Earth, and $i(r)$ is the ray take-off angle.

The ray parameter can be associated with the horizontal component of the wavenumber k_x, due to the relation:

$$p = \frac{R}{{}_n\omega_l}k_x \tag{A2}$$

and the wavenumber k_x can be defined by using normal-mode formalism

$$k_x = \frac{\sqrt{l(l+1)}}{R} \tag{A3}$$

in which l is the normal-mode angular order and R is the Earth radius. Combining eqs (A2) and (A3), we obtain

$$p = \frac{\sqrt{l(l+1)}}{{}_n\omega_l} \tag{A4}$$

from which we can compute the relationship between the angular order l and the ray parameter p:

$$l = -\frac{1}{2} + \sqrt{\frac{1}{4} + {}_n\omega_l{}^2 p^2}. \tag{A5}$$

For large l, our expression (A5) recovers eq. (5) of Zhao & Dahlen (1995) (see also Zhao & Dahlen 2007). Fixing the ray parameter, we univocally identify pairs of quantum numbers (n, l) and we obtain all of the associated normal modes that contribute to generate this seismic phase by constructive interference.

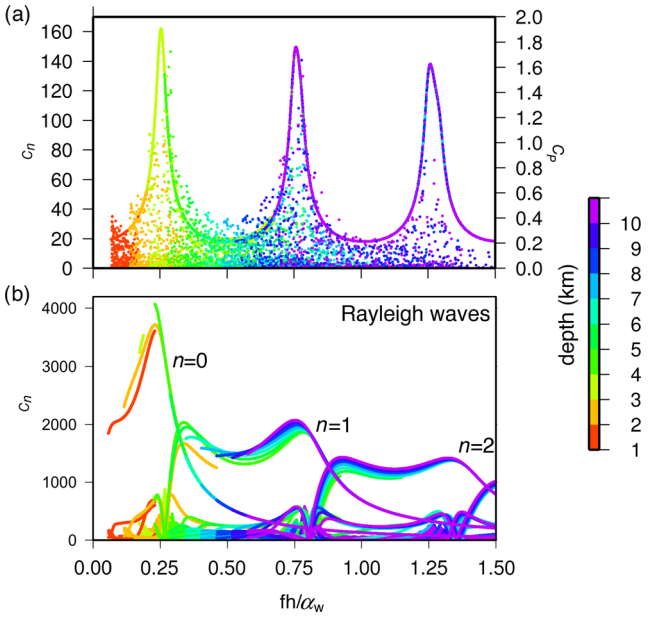


Figure A1. (a) Comparison between the results obtained using normal modes (dots) and the plane wave superposition approach (solid line) for epicentral distances between 30° and 90°. The amplitude of c_n (normal-modes approach) is shown on the left and the amplitude of c_P (plane wave superposition approach) on the right. The ocean depth is shown in colour. For computing the *P*-wave site effect using normal modes, it is necessary to integrate all of the contributions shown in this figure (dots), with each one multiplied by a phase. Small differences are due to the different earth models (PREM model with normal modes and an ocean layer over a half-space for the plane wave superposition approach). (b) Rayleigh wave site effect computed using normal modes (modified from Gualtieri *et al.* 2013).

We perform our computation for the *P* waves considering the PREM model (Dziewonski & Anderson 1981), in which we vary the ocean depth from 1 to 10 km, with discrete steps of 1 km, to simulate bathymetry. We set the period range from 4 to 10 s. We consider here all of the epicentral distances from 30° to 90°, which correspond to the *P*-wave ray parameters from $p = 0.080\,\mathrm{s\,km^{-1}}$ to $p = 0.042\,\mathrm{s\,km^{-1}}$.

In Fig. A1(a), we use dots to show the contribution to the coefficients c_n due to each mode, computed using eq. (A1). Normal modes that contribute to the *P*-wave generation are selected using eq. (A5). We plot the coefficient c_n as a function of fh/α_w, where f is the frequency, h is the ocean depth and α_w is the *P*-wave velocity in the ocean. The ocean depth is marked with colours. The actual body wave site effect can be computed by considering the summation of all c_n corresponding to the same fh/α_w, taking into account the phases.

In Fig. A1(a), we also show for comparison the site-effect coefficient obtained using the plane wave superposition approach (continuous line). The scale amplitudes on the left refer to the coefficients computed using normal modes, the scale on the right to the coefficients computed using plane wave superposition. We observe that the same ocean depth involves the same abscissa, with the same shape (dots and line colours). Moreover, the coefficients show three peaks in both cases, for the same combination of ocean depth and frequency. Differences in amplitude are due to the normal-mode normalization, whereas differences in abscissa are related to the

Downloaded from http://gji.oxfordjournals.org/ at Biblio Planets on November 2

different chosen earth models (PREM model with normal modes and an ocean layer over a half-space for the plane wave superposition approach).

By using normal modes, the same approach was used by Gualtieri *et al.* (2013) to compute the ocean site effect of the Rayleigh waves. In this case, each Rayleigh wave mode corresponds to a given radial order n. In Fig. A1(b), we plot the result for the Rayleigh waves, although as a function of fh/α_w, as we did for the body waves, instead of $\omega h/\beta_c$, like in Gualtieri *et al.* (2013). We observe that the shape of the Rayleigh wave site effect (Fig. A1b) is very different from the P-wave site effect (Fig. A1a). Then, fixing the period and the ocean depth, the site effect acts differently and the strongest sources of body and Rayleigh waves are potentially located in different geographical regions.

Downloaded from http://gji.oxfordjournals.org/ at Biblio Planets on November 2, 2016